Journal of Energy Storage 61 (2023) 106785

Contents lists available at ScienceDirect

Journal of Energy Storage

journal homepage: www.elsevier.com/locate/est

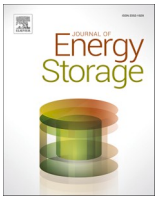

Research Papers

Numerical investigation of a plate heat exchanger thermal energy storage system with phase change material

Mehrdad Taghavi *, Minna Poikelispää, Vaibhav Agrawal, Seppo Syrjälä, Tero Joronen

Tampere University, Korkeakoulunkatu 8, 33720 Tampere, Finland

ARTICLE INFO

Keywords:
Thermal energy storage
Computational fluid dynamics
Phase change material
Plate heat exchanger
Numerical analysis

ABSTRACT

Plate-type thermal energy storage systems (PTESs) have been proposed to mitigate the effect of the low thermal conductivity of phase change materials on the performance and efficiency of thermal energy storage systems. Nevertheless, a prompt reduction in the thermal power of PTESs due to the drop/rise in the outlet temperature at the early stage of the charging/discharging process has not been well resolved. To remedy this, the current study proposes a modified PTES and presents a computational fluid dynamics model of this PTES for performance and efficiency analysis. The results show that the outlet temperature of the modified PTES is constant for 100 min in the melting and 33 min in the solidification processes, while this temperature drops/raises almost immediately in the similar PTESs after starting these processes. In addition, the presented PTES shows an improvement of 75 % and 28.6 %, respectively, in the energy storage capacity per unit volume and effectiveness than a roll-bonded PTES.

1. Introduction

Thermal energy storage systems (TESs) are applied for the energy efficiency enhancement of heating and/or cooling systems in buildings [1], solar heating systems [2,3], waste heat recovery units [4,5], and air conditioning systems [6,7]. Liu et al. [8] have claimed that using TES with a night ventilation system leads to a drop in hours of discomfort of 16 %. A study carried out by Wadhawan et al. [9] illustrates that using a TES increases the output air temperature and friction factor in a solar air heater by 86.4 % and 36.4 %, respectively. Moreover, using TES in a building's structure decreases energy consumption for air heating and cooling by up to 13 %. This efficiency increment not only reduces energy costs [10] but also decreases CO_2 emissions caused by air conditioning systems, as using TES with refrigeration appliances can reduce CO_2 emissions by 25–125 kg/MWh for cooling processes [11,12].

Most TESs rely on phase change materials (PCMs) as storing energy in the form of latent heat significantly decreases the volume of TESs [13]. However, these materials mostly have low thermal conductivity, k, which causes a rapid increase in the HTF outlet temperature, T_e, after starting the melting process [14].

According to Eq. 1, which obtains TES effectiveness, ε, using T_e, HTF inlet temperature, T_i, and initial temperature of PCM, T_{ini}, as

$$\varepsilon = \frac{T_i - T_e}{T_i - T_{ini}}, \tag{1}$$

this increase in T_e leads to a TES efficiency drop [15]. For the same reason in the solidification process, the stored energy cannot be released efficiently from the PCM to the HTF, leading to the rapid reduction in T_e, and consequently, TES effectiveness.

Other than effectiveness, the heat transfer rate or thermal power of a TES, $\dot{q}$, which is calculated as

$$\dot{q}(t) = \dot{m}_h C_{P(h)} (T_e(t) - T_i), \tag{2}$$

is used to evaluate TES performance. In this equation, $\dot{m}_h$ and $C_{P(h)}$ present the HTF mass flow rate and specific heat capacity, respectively. Similar to effectiveness, Eq. 2 shows that reducing the difference between T_e and T_i drops the TES thermal power.

Heat transfer surface enhancement in TESs is considered a practical solution to defer T_e change in the processes. Kothari et al. [16] have studied a finned PCM-based heat sink, and the results show that the fins decrease the melting time by 44 % compared to a heat sink with no fins. However, the outcomes of this study also illustrate a significant temperature difference along the fins causes poor temperature distribution in the PCM.

Plate-type thermal energy storage systems (PTESs) are another presented solution to improve the heat transfer. Unlike TESs with fins, the

* Corresponding author.
E-mail address: mehrdad.taghavi@tuni.fi (M. Taghavi).

https://doi.org/10.1016/j.est.2023.106785
Received 4 May 2022; Received in revised form 22 January 2023; Accepted 27 January 2023
Available online 8 February 2023

Nomenclature

$\dot{m}$	flow rate (kg/s)
$\dot{q}$	heat transfer rate (kJ/s)
l	latent heat (kJ/kg)
$\overrightarrow{g}$	gravitational acceleration
$\overrightarrow{s}$	source term
$\overrightarrow{u}$	velocity vector
A_{mushy}	mushy zone constant
A_c	channel cross-sectional area (m^2)
A_P	cross-sectional area of plate heat exchanger port (m^2)
C_p	specific heat capacity (kJ/kg·°K)
d	thickness of PCM section (mm)
d_h	channel hydraulic diameter (m)
e	thickness of HTF section (mm)
F	efficiency
f	liquid fraction of PCM
H	total enthalpy (kJ/kg)
h	sensible enthalpy (kJ/kg)
k	thermal conductivity (W/m·°K)
L	total latent heat of PCM (kJ/kg)
l_{ch}	length of the channel (m)
M	mass (kg)
m^2	flow maldistribution parameter
n	number of channels per fluid
P	pressure (kPa)
Q	stored/released energy (kJ)
Q_v	thermal storage capacity per unit of volume (kJ/m^3)
Re	Reynolds number
T	temperature (°K)
t	time (s)
V	volume (m^3)
v_c	non-dimensional channel velocity
v_h	velocity of HTF (m/s)
v_{PCM}	non-dimensional PCM volume
z	non-dimensional axial location

Greek symbols

δ	relative error
ε	effectiveness
μ	viscosity (kg/m·s)
$\bar{\varepsilon}$	average effectiveness
ρ	density (kg/m^3)

Subscripts

e	HTF outlet condition
h	heat transfer fluid
i	HTF inlet condition
m	melting process
s	solidification process
CFD	computational fluid dynamics
ini	initial condition
st	steel
EXP	experiment
PCM	phase change material
ref	reference

Superscripts

l	liquid phase
s	solid phase

heat transfer surface in PTESs is surrounded by both HTF and PCM, which provides more homogeneous temperature distribution in the PCM. Stathopoulos et al. and Larrinaga et al. [17,18] have presented PTESs that include several aluminium containers in a HTF vessel. Similar to these studies, Kumirai et al. [19] have carried out an experimental analysis on a plate-encapsulated TES in a ventilation system. Since these capsules have lower manufacturing costs than the containers, this PTES is more affordable in comparison with PTESs with the containers.

Despite the significant increment of the heat transfer surface in such PTESs in comparison with fined TESs, there is a serious risk of deformation in the containers or capsules due to the massive volume change of the PCMs during the phase change process [20]. Furthermore, these PTESs still have a high rate of Te change shortly after starting the melting or solidification process, which restricts their capacity to provide the demanded heating/cooling loads with a constant temperature. Since the storage capacity of these PTESs depends on the volume of the vessel, changing this capacity requires a new vessel that imposes additional costs on the system.

Saeed et al. [21] have proposed parallel roll-bonded plates in a thermal energy storage vessel in which paraffin, hexadecane ($C_{16}H_{34}$), works as the PCM and water as the HTF. A similar PTES with roll-bonded plates was also presented by Lin et al. [22] to study effectiveness, HTF outlet temperature, and thermal power over time with various flow rates. In these TESs, the PCM is stored in a vessel in which the plates are completely surrounded by the PCM. Having a gap between the plates and the upper wall of the vessel, the PCM expansion can be controlled in this PTES. According to the results of this study, compact parallel roll-bonded plates in a thermal energy storage vessel improve the effectiveness of the TES by 83.1 % despite the low thermal conductivity of the utilized PCM. Other than effectiveness enhancement and low risk of PCM section deformation, these PTESs have significantly lower manufacturing costs compared to the PTES with a container.

Despite the significant advantages of the proposed roll-bonded PTESs, the studies show that T_e changes almost immediately after starting the melting or solidification process result in significant thermal power loss. Similar to the PTESs with a container and capsule, roll-bonded PTESs have poor flexibility in thermal power capacity. Furthermore, there are some gaps between the plates and the vessel walls in roll-bonded PTESs in which heat is barely transferred, causing thermal capacity waste. Hence, an efficient PTES with a more stable T_e and less capacity waste is needed. In addition, the system should be flexible in thermal capacity without costly changes to the structure of the TES.

Gürel has studied the melting process of paraffin in a plate heat exchanger (PHE) using a two-dimensional computational fluid dynamics (CFD) model and claimed that this type of PTES decreases the melting process time by 75 % compared to a cylindrical TES [23]. Despite the good agreement between the experiments and the CFD model, two-dimensional models of a PTES are not reliable as the phase change rate of PCM is different along each cross-sectional area of the PTES [24]. Furthermore, HTF flow in these models has been simplified to a homogeneous fully developed flow in the HTF sections, while studies show that HTF pressure on the PHE plates is non-uniform [25,26].

With the aim of producing a reliable, thermal capacity flexible, and cost-effective PTES, this study presents a simplified, economical, and efficient plate heat exchanger thermal energy storage system (PHETES), which is depicted in Fig. 1. Due to the low rate of T_e changes, the PHETES has a greater effectiveness and more stable thermal power than other similar PTESs. Unlike the roll-bonded PTESs [21,22], there is no storage capacity waste in the PHETES, since the gap between the sidewalls and the plates is removed by replacing the vessel with heat

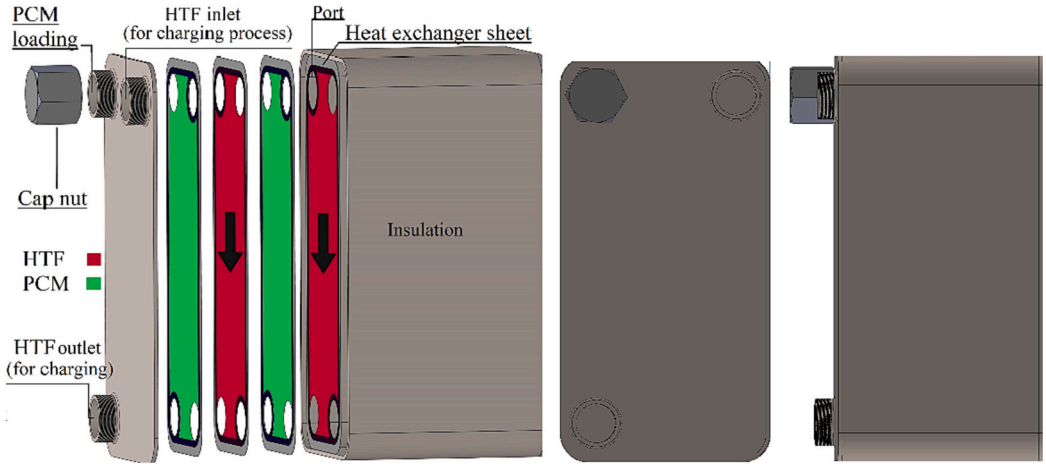

Fig. 1. Schematic of the proposed PHETES in this study.

exchange sheets in the presented system. Other than the efficiency aspect, removing the vessel in the PHETES makes this system more flexible in storage capacity change, as the PHETES can meet different capacities only by changing the number of plates.

To present a reliable method for analyzing the proposed PHETES, a three-dimensional (3D) CFD model of this PTES is presented in the current study. Unlike other presented models of PTESs, this model simulates the processes in all dimensions of the system and depicts a real flow path of the HTF flow. To further improve the CFD model, the thermophysical properties of the utilized PCM in this study are obtained from experimental investigations.

In this paper, we achieve 84.6 % effectiveness in the proposed PHETES. Furthermore, the PHETES has more stable thermal power than similar PTESs.

As the primary aim of this study, the presented model is validated with experiments. Afterward, the model will be used to analyze the performance and efficiency of the PHETES with different geometries and compare the PHETES with the roll-bonded PTES presented by Saeed et al. [21].

2. Materials and methods

The proposed PHETES comprises two main parts, i.e., the HTF and PCM parts, and each part includes several sections that are connected through the ports as can be seen in Fig. 1. This structure provides a significant heat transfer surface between the working fluids that defers T_e change during melting the PCM (charging process) and freezing paraffin (discharging process). According to Eq. 1, this delay leads to an enhancement the in effectiveness of the TES.

In this study, the PHETES is designed to work with a heat pump for space heating and supplying hot water in a residential building. Ergo, the utilized PCM in this PHETES is chosen according to the optimum operating condition of heat pumps [27,28]. To meet this condition in the PHETES, RT64HC paraffin wax from Rubitherm GmbH with a melting

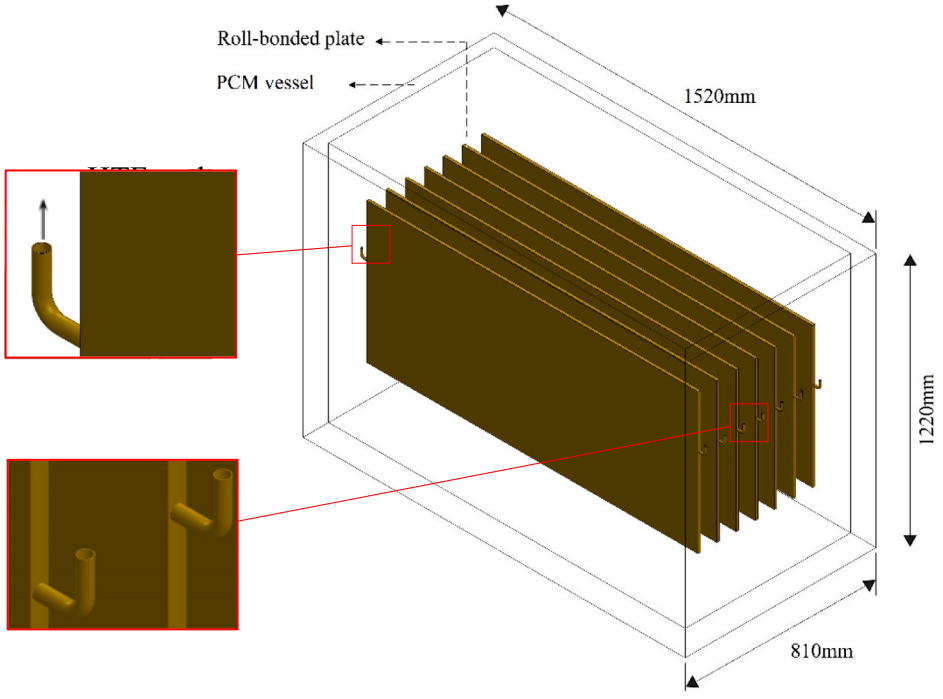

Fig. 2. Schematic of the roll-bonded plate-type thermal energy storage presented by Saeed et al. [21].

Table 1
Operating conditions of the PHETES and roll-bonded PTES in the comparison study.

Process	T_i (°C)	T_{ini} (°C)	$\dot{m}_h$ (kg/s)	$T_i - T_m$ (°C)	$T_{ini} - T_m$ (°C)	$T_i - T_s$ (°C)	$T_{ini} - T_s$ (°C)
PHETES-melting	84.2	64	0.378	16.7	−3.5	–	–
Roll-bonded PTES-melting	35	14.8	0.378	16.7	−3.5	–	–
PHETES-solidification	54	66.5	0.378	–	–	−5.5	7
Roll-bonded PTES-solidification	10	22.5	0.378	–	–	−5.5	7

range of 63–65 °C was used as the PCM.

Since this study compares the PHETES with the roll-bonded PTES [21], the dimensions of PHETES are defined according to the presented details of the roll-bonded PTES in Fig. 2. Moreover, as PCMs with different melting temperatures, T_m, and solidification temperatures, T_s, are used in the PHETES and roll-bonded PTES, values of $T_{ini} - T_m$, $T_{ini} - T_s$, $T_i - T_m$, and $T_i - T_s$ in the PHETES are defined the same as for roll-bonded PTES (Table 1) to make a fair comparison.

As seen in Fig. 1, the HTF and PCM sections in the PHETES are completely covered with heat exchange sheets, which limits the measuring temperature distribution of these sections in experimental investigations. To overcome this problem, the prototypes of the PHETES which are used for the experiments, and the CFD models comprise only one PCM and one HTF section of the presented PHETES as it is depicted in Fig. 3. This simplification not only facilitates measuring the temperature distribution in the experiments but also reduces the calculation time in the CFD simulation. However, the results of studying these prototypes are valid for the whole PHETES when the HTF flow is distributed uniformly between the sections.

To detect a uniform HTF flow distribution between the plates in a PHE, if values of non-dimensional channel velocity, v_c, which is obtained as

$$v_c = \left(\frac{A_P}{n \bullet A_c}\right) m \cdot \frac{coshm(1-z)}{sinhm}, \tag{3}$$

are close to one, the distribution can be assumed to be uniform [29,30]. In this equation, A_p, n, A_c, and z, stand for the cross-sectional area of the port in a PHE, the number of channels per fluid, the cross-sectional area of channels, and the non-dimensional axial location along the port, respectively [29]. Parameter m in Eq. 3 is calculated as

$$m^2 = 0.94 \frac{d_h}{l_{ch}} Re^{0.145} \left(\frac{nA_c}{A_P}\right)^2, \tag{4}$$

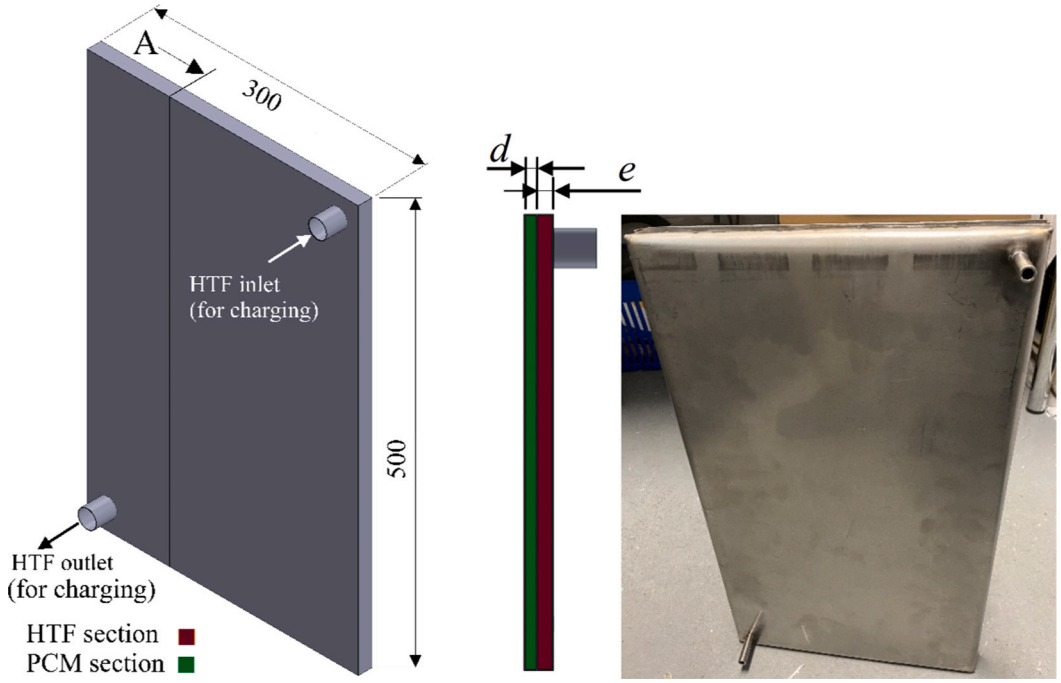

(c) Table of the geometries details

	e (mm)	d (mm)	$\frac{V_{PCM}}{V_{total}}$	$\dot{m}_h$ (kg/s)	v_h (m/s)	CFD	Experiments
Geometry 1	40	30	0.41	0.01	$8.3e^{-4}$	✓	✓
Geometry 2	20	10	0.31	0.005	$8.3e^{-4}$	✓	✓
Geometry 3	10	10	0.45	0.003	0.001	✓	×

Fig. 3. Prototype of the proposed PHETES for CFD and experimental studies with one PCM and one HTF section. (a) Schematic, (b) image, and (c) table of geometries details.

where m^2 is the flow maldistribution parameter, d_h is the hydraulic diameter of the channel, l_{ch} is the length of the channel, and Re is the Reynolds number [31,32].

In this study, three geometries of the PHETES prototype with different thicknesses of PCM and HTF sections are designed according to the presented properties shown in Fig. 3. Using the presented thicknesses in Geometries 1, 2, and 3, the PHETES comprises 10, 20, and 30 sections, respectively. According to the presented details in Fig. 3, values of v_c are calculated for each design. The results show that the obtained values of v_c for Geometries 1, 2, and 3 are 1, 1.04, and 1.06, respectively. Hence, as these values are close to one, the flow distribution between the sections can be assumed to be uniform, and consequently, the outcomes of studying the prototypes with one PCM and HTF section are valid for the whole proposed PHETES, which has several sections. Moreover, the dimensions and HTF flow rate of the prototype are reduced by three times in order to decrease the numerical calculations time and simplify the experimental setup.

The CFD model is created using the presented geometries in Fig. 3, and this model is validated with an experimental analysis on the prototypes with Geometries 1 and 2. This validation is carried out by comparing the obtained temperature distribution in the PHETES and the HTF outlet temperature from the simulation with the experiments. Using Geometry 1, the validity of the presented model with different HTF flow rates and inlet temperatures is analyzed, and in Geometry 2, the effect of changing the thickness of the sections on the model accuracy is studied. After the validation, the geometries are compared with each other considering the PCM phase change rate, the profile of T_e, effectiveness, and efficiency using the CFD model. Accordingly, the geometry that has the better performance in the mentioned parameters is chosen to be compared with the roll-bonded PTES, which is depicted in Fig. 2.

Among the crucial parameters to analyze a TES [17], T_e and temperature distribution in the PCM and HTF sections are obtained directly from the CFD model. Total thermal storage capacity, Q_{total}, and storage capacity per unit of volume, Q_v, are calculated as

$$Q_{total} = M_{PCM}\left[C^{s}_{p(PCM)}(T_m - T_{ini}) + C^{l}_{p(PCM)}(T_i - T_m)\right] + M_h C_{p(h)}(T_i - T_{ini}) + M_{st} C_{p(st)}(T_i - T_{ini}) + M_{PCM}\Delta H, \quad (5)$$

and $Q_v = \frac{Q_{total}}{V}$. In these equations, M_{PCM}, M_h, and M_{st} are the mass of the PCM, HTF, and heat exchange sheets, respectively, and ΔH presents the latent heat of the PCM. Superscripts s and l also stand for solid phase and liquid phase.

The profile of the stored/released energy or thermal power per unit of volume is given by

$$Q_v(t) = \frac{\int_0^t \dot{q}(t)\,dt}{V}, \quad (6)$$

in which V is the total volume of PHETES and t denotes time. Since the HTF section in the PHETES works as a tank, the Abdoly and Rapp method [33] is used in this study to analyze the performance of the PHETES. In this method, recovered energy from the PHETES is considered useful until the changes in T_e are <20 % of the initial temperature. Accordingly, the recovered energy of a TES is given as

$$Q(t) = \begin{cases} 0 & , if \ \frac{T_e - T_i}{T_{ini} - T_i} < 0.8, \\ M_h C_{P(h)}(T_e - T_i), & if \ \frac{T_e - T_i}{T_{ini} - T_i} \geq 0.8, \end{cases} \quad (7)$$

and efficiency of the TES, $F(t)$, is obtained as

$$F(t) = \frac{\sum Q(t)}{Q_{total}}. \quad (8)$$

As phase change in TESs is a transient process, the average effectiveness, ε, of a TES in the charging or discharging process is calculated using the following equation

$$\bar{\varepsilon}(t) = \frac{\int_0^t \left(\frac{T_e - T_i}{T_{ini} - T_i}\right) dt}{t}, \quad (9)$$

to analyze the performance of the TES during the whole process [34]. According to Eq. 9, the values of ε are bounded between 0 and 1.

3. Experimental setup and procedures

The experiments are categorized into two main sections. The first section gives the thermophysical properties of the utilized PCM, i.e., phase-change temperature, specific heat capacity, thermal conductivity, and viscosity to enhance the accuracy of the CFD model. The second part consists of performing experiments on the PHETES prototype, which is presented in Fig. 3.

3.1. PCM thermophysical properties analysis

The thermal conductivity of the PCM in the solid phase was analyzed using a Netzsch LFA 467 laser flash analyzer by which the thermal diffusivity of the paraffin was measured. Then, the thermal conductivity was calculated as $k = \alpha\rho C_p$, in which α and ρ denote thermal diffusivity and density, respectively [35].

For the liquid phase, the obtained profile of thermal conductivity with respect to the temperature in the solid phase was compared with a study on the thermal conductivity of paraffin wax (PW) [36]. Then, by following the PW profile in the liquid phase, the values of the thermal conductivity of RT64HC in the liquid phase were calculated. The specific heat capacity of the PCM was determined using Netzsch DSC Polyma 214 differential scanning calorimetry. Phase-change temperatures (melting and crystallization) were determined using DSC with two heating cycles from 0 °C to 100 °C in an N_2 atmosphere and a heating and cooling rate of 10 K/min.

Using the acquired data from experimental analysis on the utilized PCM in the PHETES, the PCM thermophysical properties are shown in Table 2.

3.2. PHETES experimental setup

Details of the experimental setup to validate the CFD model can be found in Fig. 4. In order to minimize the heat loss from the unit, the outer walls and the hoses were insulated. The placement of five temperature sensors on the HTF section and four sensors on the PCM provided a comprehensive analysis of temperature distribution in the PHETES sections. Due to technical restrictions with putting the sensors inside the sections, the sensors were placed on the outer walls of the prototypes. The accuracy of the utilized circulation unit and Pt-100 sensors in this setup were ±0.5 °C and ±0.35 °C, respectively, according to the presented datasheet by the suppliers and the performed calibration before starting the experiments.

The experiments were carried out in five sections as listed in Table 3. Through test sections 1 and 2, the accuracy of the model with different

Table 2
Thermophysical properties of RT64HC paraffin wax as the PCM in the PHETES.

T_m (°C)	T_s (°C)	ΔH (kJ/kg)	C_p (kJ/kg °K)	Density solid/liquid (kg/m^3)	k (W/m °K)	μ (Pa·s)
64	59.5	270	2–29.62	880/780	0.22–0.34	0.01307–0.01105–0.0097–0.00806

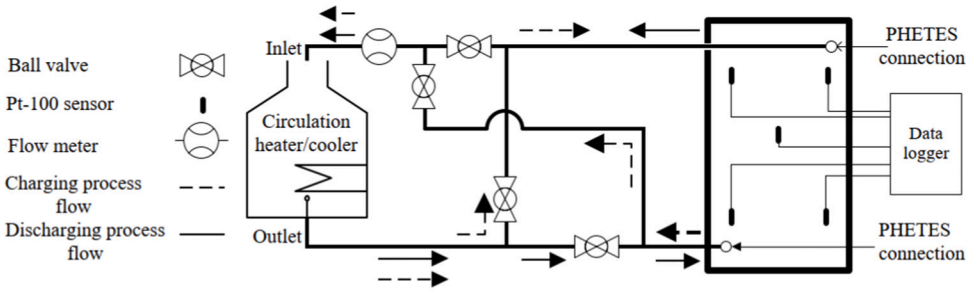

(a) Schematic of the experimental setup.

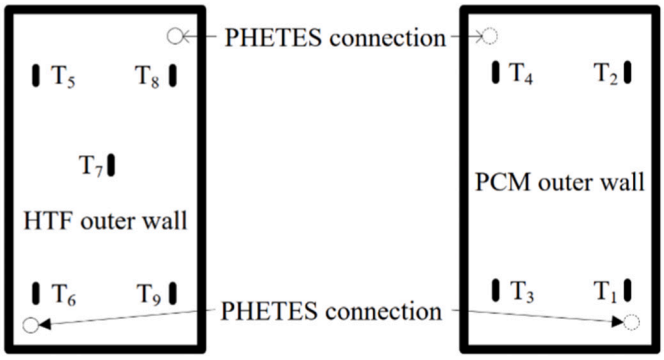

(b) Location of temperature sensors on the PHETES.

(c) PHETES laboratory setup.

Fig. 4. Experimental facilities to analyze the PHETES prototypes.

Table 3
Details of the test sections to validate the CFD model.

Test section	Geometry and process	T_i (°C)	$\dot{m}_h$ (kg/s)	T_{ini} (°C)
1	Geometry 1, charging	78	0.01	29
2	Geometry 1, charging	78	0.02	20
3	Geometry 1, discharging	20	0.01	75
4	Geometry 1, discharging	30	0.01	75
5	Geometry 2, charging	78	0.01	20

HTF flow rates was evaluated, and using test sections 3 and 4, the effect of working temperature on the model accuracy was studied. Test section 5 was used for validating the model with different HTF and PCM thicknesses. To evaluate the repeatability of these experiments, all the test sections were carried out twice and the results were compared with each other.

In cases with less than a 5 % difference between the results, the first test outcomes were used for the validation. However, when the difference exceeded 5 %, the test was repeated a third time and the average values were considered.

To detect the appropriate flow direction in the PHETES for the charging and discharging processes, the upward and downward flow directions are compared in Fig. 5 considering the thermal power profile. According to Fig. 5(a), thermal power in the upward charging process dropped immediately after starting the test, while thermal power was almost constant for a longer time using the downward flow in this process. Unlike the charging process, upward flow can provide more stable thermal power in discharging process according to Fig. 5(b).

Hence, the downward flow for the charging process and the upward flow for discharging were chosen in this study.

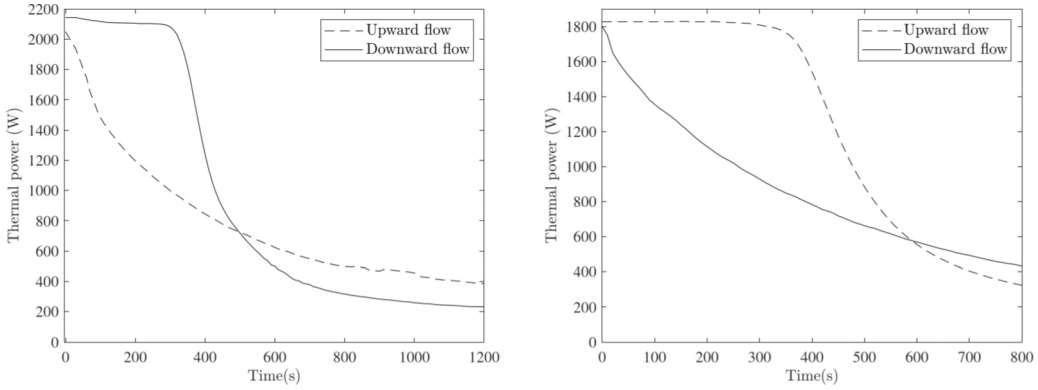

(a) Charging process. (b) Discharging process.

Fig. 5. Comparing the thermal power of the PHETES with the upward and downward HTF flow direction in the charging and discharging processes.

4. Numerical model

Numerical analysis in the current study was performed using ANSYS-Fluent 2019 R3. The governing equations to analyze the transient heat transfer, phase change, and fluid flow are continuity,

$$\frac{\partial \rho}{\partial t} + \nabla \bullet (\rho \vec{u}) = 0, \tag{10}$$

momentum,

$$\frac{\partial \rho \vec{u}}{\partial t} + \nabla \bullet (\rho \vec{u}\vec{u}) = -\nabla P + \mu(\nabla^2 \vec{u}) + \rho \vec{g} + S, \tag{11}$$

and energy,

$$\frac{\partial (\rho H)}{\partial t} + \nabla \bullet (\rho \vec{u} H) = \nabla \bullet \left(\frac{k}{C_p} \nabla h\right) S_h, \tag{12}$$

in which ρ, H, $\vec{u}$, P, $\vec{g}$, and S_h denote density, enthalpy, velocity vector, pressure, gravitational acceleration, and energy source term, respectively [37]. In addition, parameter S in the momentum equation is the momentum reference term, which is obtained from

$$S = \frac{(1-f)^2}{f^3} A_{mushy} \vec{u}, \tag{13}$$

where A_{mushy} is the mushy zone constant and equals 10^5 in this study [38]. Parameter f in Eq. 13 is the liquid fraction of the PCM and is calculated as

$$f = \begin{cases} 0 & , \text{if } T < T_{solidus}, \\ 1 & , \text{if } T > T_{liquidus}, \\ \dfrac{T - T_{\text{solidus}}}{T_{\text{liquidus}} - T_{\text{solidus}}} & , \text{if } T_{solidus} < T < T_{liquidus}. \end{cases} \tag{14}$$

Since values of PCM enthalpy in TESs are affected by phase and temperature changes, both sensible enthalpy, h, and latent heat enthalpy were considered to calculate PCM enthalpy [39] using the equations

$$H = h + l \tag{15}$$

and

$$h = h_{\text{ref}} + \int_{T_{\text{ref}}}^{T} C_{\text{P}}\, dt. \tag{16}$$

The reference state in Eq. 16 is defined as the initial condition of the TES before starting the processes. Unlike sensible enthalpy, latent heat enthalpy in this study only relates to the PCM, as there is no phase change in the HTF section during the processes. Thus, l in Eq. 15 equals zero for HTF and the heat exchange sheets in the PHETES. Since phase change in the PCM occurs gradually, l is defined as a function of the PCM liquid fraction and total latent heat and calculated as $l = f \cdot L$, where L represents the total latent heat [23].

To model density changes of the PCM due to the phase change process, the Boussinesq model was used in the numerical analysis [23]. Having a Reynolds number of <2000 in this study, the laminar viscous model was used for the CFD model. The SIMPLE algorithm was used in the solution methods, the PRESTO model for the pressure validation equation, and the second-order upwind solution method for energy and momentum equations [40]. To enhance the accuracy of the model, the under-relaxation factors for pressure correction, density, body forces, momentum, liquid fraction, and energy were equal to 0.5, 1, 0.9, 0.68, 0.9, and 1, respectively. In addition, the convergence criteria for continuity, momentum, and energy equations were defined as 10^{-8}, 10^{-8}, and 10^{-14}, respectively [40]. For validating the proposed model, the relative error, δ, of the model results from the experiments was calculated as

$$\delta = \frac{|T_{\text{EXP}} - T_{\text{CFD}}|}{T_{\text{EXP}}} \times 100\%, \tag{17}$$

where T_{CFD} denotes the given temperature values from the CFD model and T_{EXP} is the measured temperature from the experiments [41]. To analyze the model accuracy for the whole process, the average of the

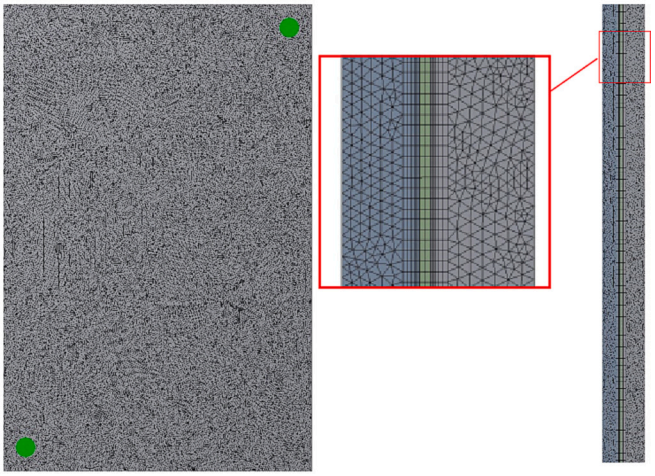

Fig. 6. Numerical mesh construct of the PHETES.

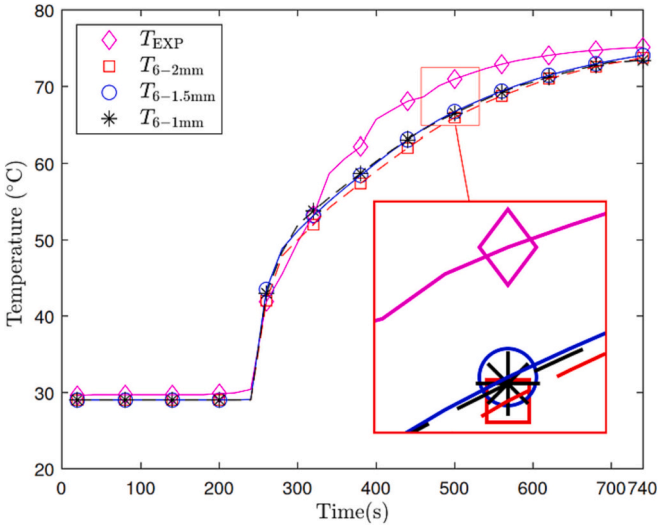

Fig. 7. Temperature profile at T_6 obtained from the experiments and CFD model with different mesh sizes during the charging process.

relative error was obtained as $\bar{\delta} = \frac{\int_0^t \delta \, dt}{t}$.

Fig. 6 depicts the mesh structure of the PHETES in the numerical model. To study the effect of mesh element size on the accuracy of the model and find the appropriate size considering the accuracy and calculation time, three CFD models with mesh element sizes of 2 mm, 1.5 mm, and 1 mm were created. Then, the values of T6 obtained from the models were compared with the experiments during the melting process, as can be seen in Fig. 7. Accordingly, δ_{max} for mesh sizes of 1 mm, 1.5 mm, and 2 mm, were 0.0822, 0.0853, and 0.1016, respectively. In addition, $\bar{\delta}$ for these mesh sizes were 0.0396, 0.03974, and 0.04406. Hence, it can be seen from these results that increasing the mesh size from 1 mm to 2 mm had no significant effect on the accuracy of the model. As a result, the CFD model with a 2 mm mesh size was selected to reduce the calculation time.

5. Results and discussion

The CFD model validation is analyzed in the first section of the results part. Section 5.2 discusses the effect of the geometries on the performance of the PHETES, and Section 5.3 compares the PHETES' performance with that of the roll-bonded PTES [21].

5.1. Numerical model validation

The temperature distributions in Geometry 1 obtained from the

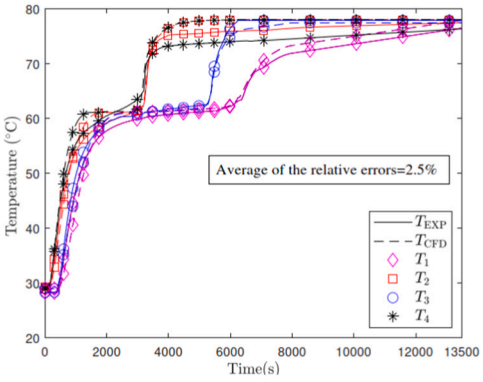

(a) PCM part temperature distribution in test section 1 with $\dot{m}_h$=0.01 kg/s.

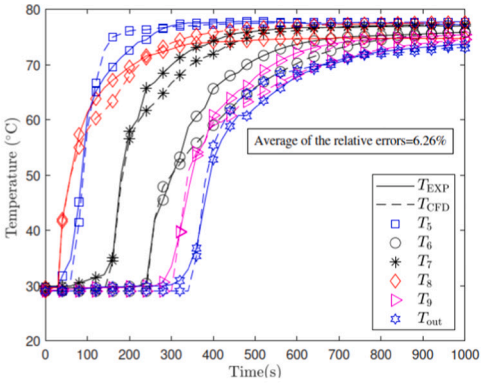

(b) HTF part temperature distribution in test section 1 with $\dot{m}_h$=0.01 kg/s.

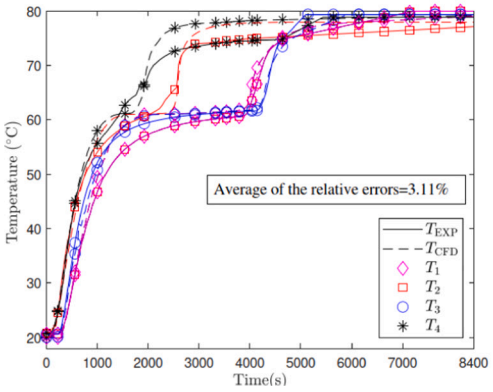

(c) PCM part temperature distribution in test section 1 with $\dot{m}_h$=0.02 kg/s.

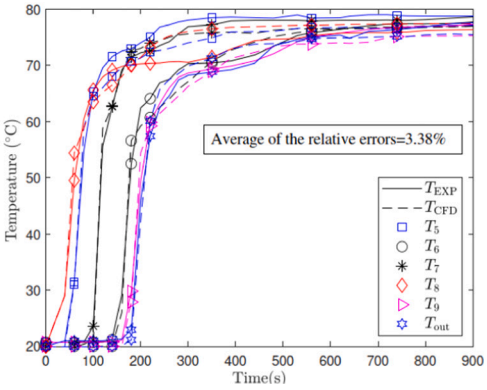

(d) HTF part temperature distribution in test section 1 with $\dot{m}_h$=0.02 kg/s.

Fig. 8. Numerical and experimental results of temperature distribution in HTF and PCM sections during the charging process with Geometry 1 and different HTF flow rate.

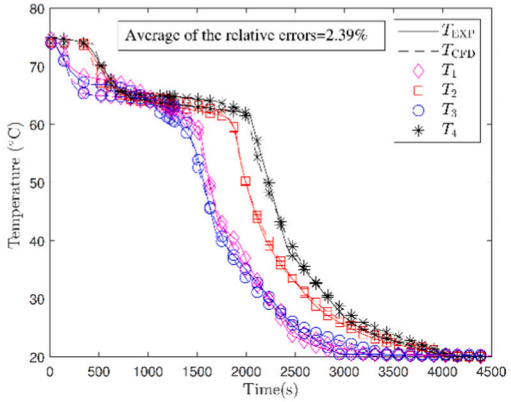

(a) PCM part temperature distribution in test section 3 with $T_i = 20$ °C.

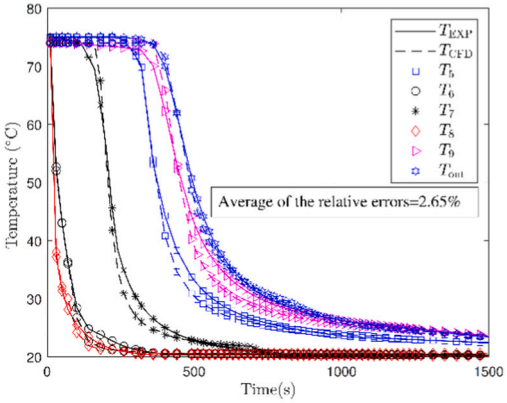

(b) HTF part temperature distribution in test section 3 with $T_i = 20$ °C.

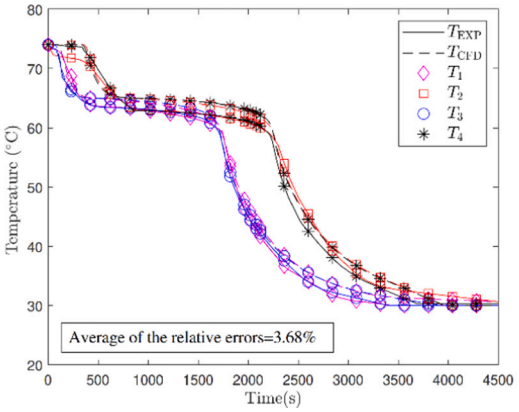

(c) PCM part temperature distribution in test section 3 with $T_i = 30$ °C.

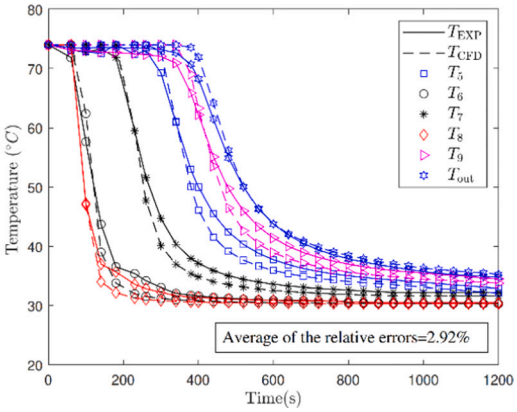

(d) HTF part temperature distribution in test section 3 with $T_i = 30$ °C.

Fig. 9. Numerical and experimental results of temperature distribution in the HTF and PCM sections in the discharging process with Geometry 1 and different inlet temperatures.

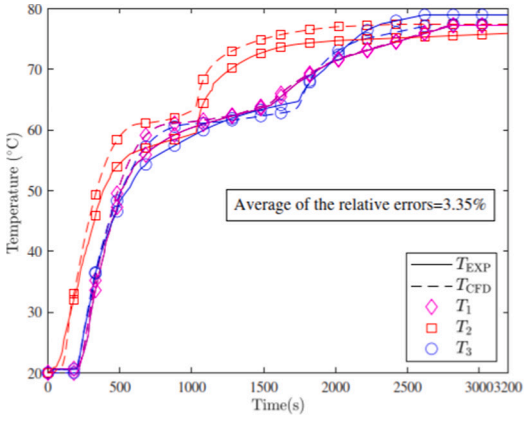

(a) Temperature distribution profile of the PCM part in test section 5.

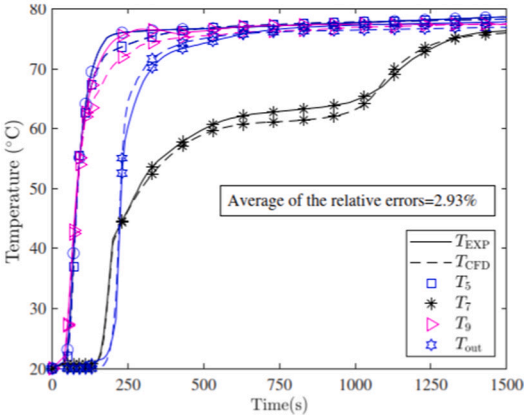

(b) Temperature distribution profile of the HTF part in test section 5.

Fig. 10. The CFD and experiments results of temperature distribution during melting processes with Geometry 2, $T_i = 78$ °C, $\dot{m}_h = 0.01$ (kg/s).

model and experiments during the charging process with $\dot{m}_h = 0.01$ kg/s and $\dot{m}_h = 0.02$ kg/s are presented in Fig. 8. This figure shows that δ values for the PCM and HTF parts in test sections 1 and 2 were 4.4 % and 3.27 %, respectively. Moreover, comparing Fig. 8(a) and (c) with Fig. 8 (b) and (d) illustrates that the HTF section had a higher $\overline{\delta}$ than the PCM section since the temperature in the HTF changes at a higher rate than the PCM due to the phase change in the PCM, in which the temperature remains constant. Finally, comparing the values of $\overline{\delta}$ in all sections of Fig. 8 shows that changing the HTF flow rate in the presented range barely affected the accuracy of the model, since there is no noticeable difference between the $\overline{\delta}$ values in test sections 1 and 2.

To analyze the effect of operating temperature changes on the model accuracy, the results of the numerical model and experiments with different T_i are presented in Fig. 9. The results show that the $\overline{\delta}$ values in test sections 3 and 4 were 2.54 % and 3.3 %, respectively. As a result, changing the operating temperature in this range had no significant effect on the accuracy of the model. Furthermore, comparing Figs. 8 and 9 illustrates that the model was reliable for both charging and discharging processes by comparing the values of $\overline{\delta}$ in these processes.

The temperature distribution profile obtained from the experiments and CFD model with Geometry 2 during the charging process is shown in Fig. 10 to study the accuracy of the model with different geometries. According to the results, $\overline{\delta}$ in Geometry 2 was 4.38 %, which is close to the obtained value in Geometry 1 with the same operating conditions (Fig. 8(a) and (b)). As a result, changing the thickness of the sections in the PHETES barely affected the reliability of the model.

The results of the validation sections illustrate that the presented model in this study is valid for the defined operating conditions and geometries. Thus, this model can be used to replace experimental investigations for further analysis.

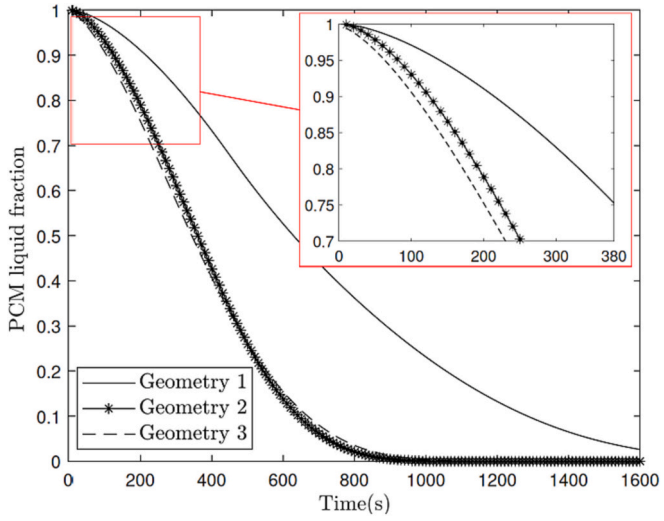

Fig. 11. PCM liquid fraction profile in the PHETES with different geometries during the discharging process.

5.2. Analyzing geometries with different v_{PCM}

The PHETES with the presented geometries in Fig. 3 was compared considering the phase change rate, energy transfer rate, thermal storage capacity, efficiency, and effectiveness to investigate the effect of v_{PCM} on the PHETES's performance.

5.2.1. PCM phase change rate

The effect of v_{PCM} on the PCM phase change rate can be analyzed using Figs. 11 and 12. According to Fig. 11, the PCM phase change rate in Geometry 1 was noticeably lower than in the other geometries. The reason can be found in Fig. 12, which compares the temperature contours of the PCM section outer wall with different geometries. Comparing Fig. 12(a) with Fig. 12(b) and (c) shows that a thick PCM section restricted conduction heat transfer in this part, as the wall temperature in the thinner PCM section geometry dropped at a higher rate than the thick PCM geometry. Thus, the stored energy in the interior sections of the thick PCM cannot be released efficiently to the HTF to dramatically drop the phase change rate.

As a result, using a thin PCM section is a feasible solution to reduce the effect of the low thermal conductivity of paraffin on the phase change rate in the PHETES.

In addition, comparing Geometries 2 and 3 using Fig. 11 reveals the fact that the phase change rate was not affected only by PCM thickness, as these two geometries had the same PCM thickness but a different PCM phase change rate. According to Fig. 3, HTF had a higher velocity on the heat transfer surface in Geometry 3 than in Geometry 2, causing a higher

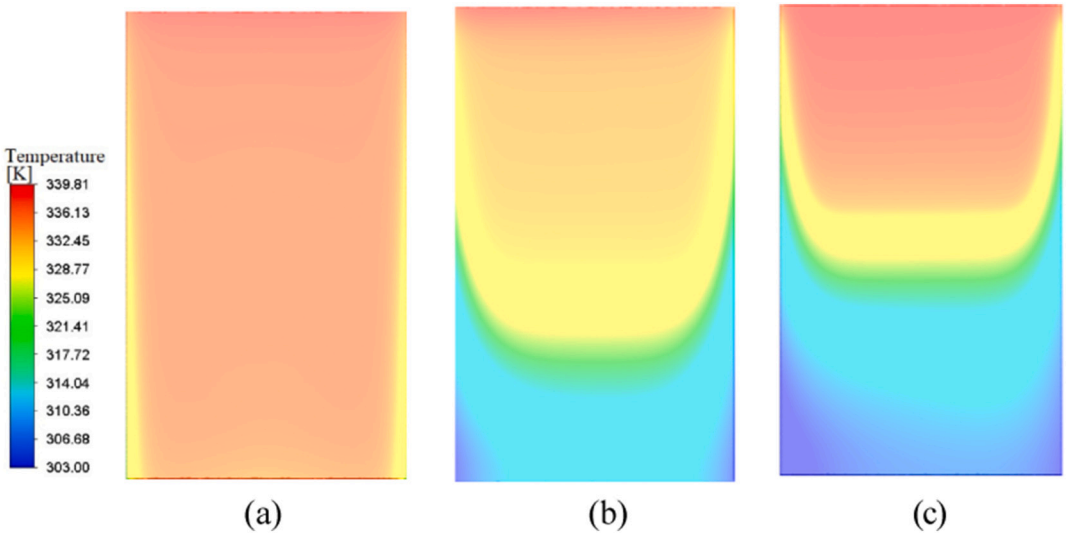

Fig. 12. Comparison temperature contours of the PCM section outer wall of the PHETES at $t = 720$ s in the discharging process for geometry 1 with the PCM section thickness = 30 mm, $v_{PCM} = 0.41$, (a), geometry 2 with PCM section thickness = 10 mm, $v_{PCM} = 0.31$ (b), and geometry 3 with PCM section thickness = 10 mm, $v_{PCM} = 0.45$, (c).

forced convection heat transfer from the PCM to HTF [42]. Hence, heat can be restored at a higher rate using Geometry 3, which increases the phase change rate.

As a result of this subsection, to enhance the phase change rate in PHETES, high values of v_{PCM} and a low thickness of HTF and PCM sections should be considered in the design process.

5.2.2. HTF outlet temperature and transferred energy

Although Geometry 1 had a lower PCM phase change rate than the other geometries, Fig. 13 illustrates that the HTF outlet temperature was constant for a longer time in this geometry. According to Fig. 3, the volume of the HTF section in Geometry 1 was higher than in the other geometries, causing greater volume storage of high-temperature HTF in this geometry during the charging process. Hence, the outlet temperature drop in Geometry 1 happened with more delay than in Geometries 2 and 3. Nevertheless, when all the accumulated HTF in Geometry 1 exited from the PHETES, the outlet temperature dropped rapidly in this geometry due to the low heat transfer rate between the PCM and HTF.

Furthermore, Fig. 13 illustrates that the temperature drop point in Geometry 2 was almost the same as in Geometry 3 despite having more stored high-temperature HTF in Geometry 2. The reason for this was a higher heat transfer rate in Geometry 3 than in Geometry 2 (according to Section 5.2.1), which compensated for the low capacity of storing HTF in this geometry.

Comparing Figs. 13 and 14 shows the effect of the T_e drop on the energy transfer rate from the PHETES. According to Eq. 2, decreasing T_e reduces the rate of energy transfer in the PHETES. Thus, as Geometry 1

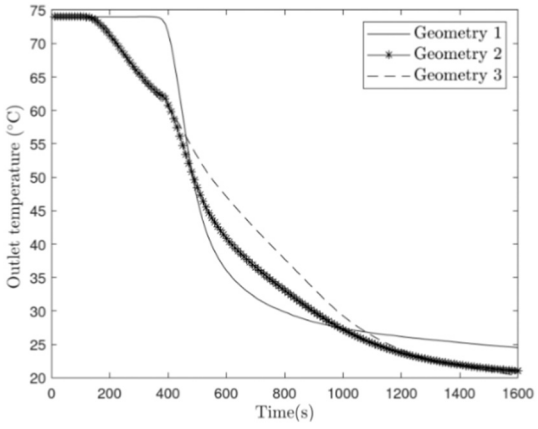

Fig. 13. HTF outlet temperature profile in the PHETES with different geometries during the discharging process.

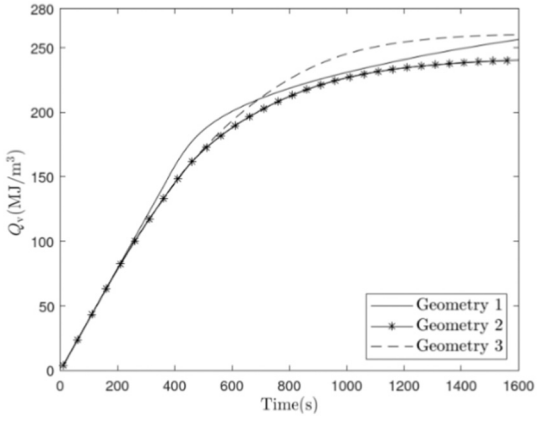

Fig. 14. Transferred energy profile over the discharging process in the PHETES with various geometries.

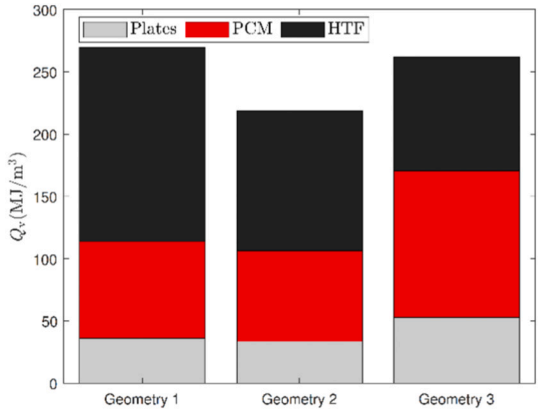

Fig. 15. PHETES' thermal energy storage capacity per volume unit with various geometries and $T_{dead} = 20$ °C.

had a constant T_e until 400 s from starting the discharging process, this geometry had a higher rate than Geometries 2 and 3 during this time. However, since T_e in Geometry 1 plunged after 400 s, the slope of the Q_v graph in this geometry dramatically decreased, which showed a noticeable drop in the thermal power of the PHETES.

Fig. 14 also illustrates that more energy per unit of volume could be restored from Geometry 3 than Geometry 2 despite having the same volume of PCM in these two geometries. The reason can be found in Fig. 15, which depicts the amount of Q_v in PHETES with $T_{dead} = 20$ °C as the dead state. According to this graph, more energy in the form of latent heat can be stored in Geometry 3, as this geometry has a higher v_{PCM} than Geometry 2. In addition, Fig. 15 shows that Geometry 1 can store more Qv than Geometry 3 since a massive amount of energy can be stored with the HTF in the form of sensible heat. Nevertheless, due to the low heat transfer rate between the PCM and HTF in Geometry 1 (concluded in Section 5.2.1), this geometry cannot release the stored energy at an appropriate rate.

5.2.3. Effectiveness and efficiency

The CFD model shows that the value of efficiency for the PHETES with Geometry 1 is 0.68, while this parameter in Geometries 2 and 3 is 0.558, and 0.4789, respectively. As can be found in these results, Geometry 1 had a higher efficiency than the other geometries due to the late T_e drop in this geometry. However, according to Eq. 7, efficiency considers the performance of PHETES as long as the outlet temperature drop is <20 % of the initial temperature, while effectiveness considers the whole process. The results of calculating the average effectiveness show that this parameter for Geometries 1, 2, and 3 equals 0.3351, 0.522, and 0.5667, respectively. These results illustrate that Geometry 3 has a significantly higher average effectiveness than Geometry 1 during the process, while the difference between Geometries 2 and 3 is <5 %.

As a result of Section 5.2, although Geometry 3 has a low value of efficiency compared to the other geometries, the PHETES with this geometry is chosen to be compared with the roll-bonded PTES due to having a higher effectiveness, energy transfer rate, and PCM phase change rate.

5.3. Comparison of the PHETES with roll-bonded PTES

According to the presented results by Saeed et al. [21] and the outcomes of this study, the performance of PHETES was compared to the roll-bonded PTES considering the HTF outlet temperature profile, energy transfer rate, thermal storage capacity, and effectiveness.

5.3.1. HTF outlet temperature changes

The HTF outlet temperature changes, which are obtained as $\Delta T = |T_e - T_i|$, show the stability of the TES to provide the demanded heating/

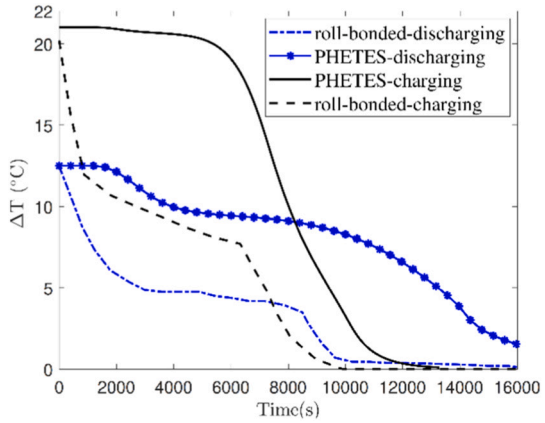

Fig. 16. HTF outlet temperature changes during the melting and solidification processes in the roll-bonded PTES and PHETES.

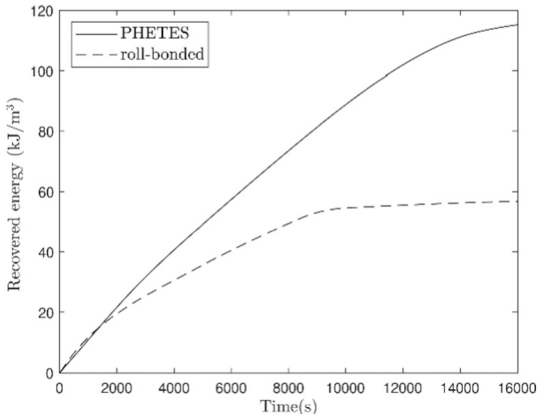

Fig. 18. Energy recovery rate from the roll-bonded PTES and the PHETES during the solidification process.

cooling loads with a constant temperature. Considering this parameter, Fig. 16 compares the PHETES with the roll-bonded PTES during the charging and discharging processes. This graph shows that T_e was constant in the PHETES for almost 33 min after starting the discharging and 100 min after starting the charging processes, while this temperature drops almost immediately in the roll-bonded PTES. The reason for this advantage is the stored HTF in the PHETES, which delays the ΔT drop in this system. Moreover, the heat transfer surface area in the roll-bonded PTES equals 26.675 m^2, while the PHETES with the same volume as the roll-bonded PTES has 116.58 m^2 of heat transfer surface area. For this reason, the PHETES has a higher rate of heat transfer between the PCM and HTF, which delays the ΔT drop in the PHETES.

5.3.2. Energy transfer rate

According to Figs. 17 and 18, which compare the rate of stored and recovered energy in the PHETES and the roll-bonded PTES, these two TESs have almost the same heat transfer rate at the beginning of both processes. However, Fig. 17 shows that after 500 s from starting the melting process, the heat transfer rate dramatically decreases in the roll-bonded PTES, while this rate in the PHETES is still constant by 8000 s. Like the melting process, Fig. 18 implies that thermal power in the PHETES is more stable than the roll-bonded PTES during the solidification process. The reason for having constant thermal power for a longer time in PHETES can be found in section 5.3.1, which concluded the PHETES has a lower ΔT drop than the roll-bonded PTES during the processes. According to Eq. 2, more delay in the ΔT drop in the PHETES increases the heat transfer rate or thermal power in this TES than the roll-bonded PTES.

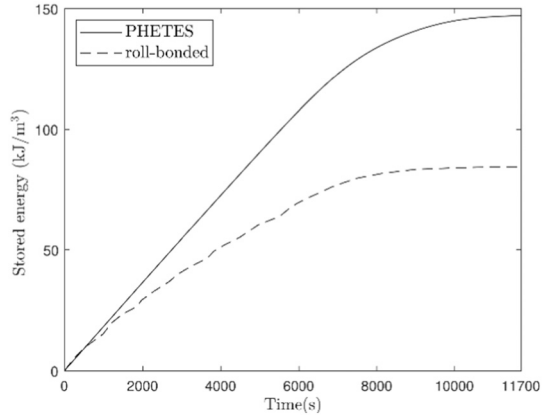

Fig. 17. Energy storage rate in the roll-bonded PTES and the PHETES during the melting process.

5.3.3. Energy storage capacity

According to the published results by Saeed et al. [21], $\nu_{PCM} = 320$ kg/m^3 in the roll-bonded PTES, while this parameter in the PHETES equals 298.5 kg/m^3.

Consequently, the roll-bonded PTES has more capacity than the PHETES to store energy. Nevertheless, Fig. 17 illustrates that the PHETES can store approximately 75 % more energy than the roll-bonded PTES. The reason for this contradiction can be described by considering the poor thermal conductivity of paraffin, particularly in the liquid phase. Since the PCM section in the roll-bonded PTES is thicker than the PHETES, more time is needed to melt all the PCM in the roll-bonded PTES. Moreover, the thermal power of the roll-bonded PTES is noticeably lower than the PHETES (according to Section 5.3.2), which decreases the rate of storing energy in the roll-bonded PTES. Ergo, the PHETES can store more energy than the roll-bonded PTES during the same time, despite having a lower thermal capacity.

In addition, the thermal capacity waste in the roll-bonded PTES due to the gaps between the plates decreases the available thermal capacity in this TES. Unlike the roll-bonded PTES, there are no side gaps in the PHETES resulting in the PHETES having more available capacity compared to the roll-bonded PTES.

As a result, the PHETES can store more heat than the roll-bonded PTES due to having a thinner PCM section and less capacity waste.

5.3.4. Effectiveness

According to the study performed by Saeed et al. [21], the average effectiveness of the roll-bonded PTES in the melting process with $T_i = 35$ °C and $\dot{m}_h = 0.378$ kg/s equals 56 %, while this parameter for the PHETES with the same operating conditions is 84.6 %. The reason for the PHETES having a higher effectiveness can be found in Fig. 16, which shows that ΔT in the PHETES drops at a lower rate than the roll-bonded PTES in both processes. According to Eq. 1, since $T_{ini} - T_i$ is almost the same in both TESs, the PHETES has more effectiveness than the roll-bonded PTES due to having a constant ΔT for a longer time.

In the presented study, only three geometries of the PHETES with different PCM and HTF sections are studied. However, to present an optimized geometry, all the effective parameters on the performance and efficiency of the PTESs must be studied. Hence, enhancing the presented PHETES using an optimized method is the next scope of the presented study.

6. Conclusion

This study presented a simplified, cost-effective, and efficient design of a plate heat exchanger thermal energy storage system and compared the performance and efficiency of this system with a roll-bonded plate thermal energy storage system. The main outcomes of the study are itemized below:

- Considering thermal power, downward HTF flow for the charging and upward flow for the discharging process are proposed in the presented HETES.
- While the temperature in the roll-bonded PTES drops or rises rapidly after starting the processes, storing HTF in the PHETES stabilizes the outlet temperature of this TES for a longer time than the roll-bonded PTES as this temperature is almost constant for 100 min and 33 min, respectively, during the melting and solidification processes in the PHETES.
- The PHETES has a 75 % higher thermal storage capacity per unit of volume than the roll-bonded PTES, despite having less PCM. Therefore, using the PHETES significantly decreases the size of the unit, which is beneficial for systems with space restrictions.
- Increasing the ratio of the PCM volume to the total volume of the PHETES enhances the thermal capacity of the system. Nevertheless, raising this parameter to >0.45 reduces the capacity due to the reduction of the stored energy in the HTF section.
- Due to having a constant HTF outlet temperature for a longer time in the PHETES, the average effectiveness in the PHETES is 28.6 % higher compared to the roll-bonded PTES with the same operating conditions.
- The flexibility of the PHETES to quickly meet various thermal capacities due to the simplified design makes this system profitable for heating/cooling systems with the possibility of capacity change.

Declaration of competing interest

The authors declare that they have no known competing financial interests or personal relationships that could have appeared to influence the work reported in this paper.

Data availability

Data will be made available on request.

Acknowledgments

This work was supported financially by the Paavo V. Suominen Fund for Industrial Research at Tampere University. We are also grateful to Maria Goossens, who greatly assisted this research.

References

[1] S.R.L. da Cunha, J.L.B. de Aguiar, Phase change materials and energy efficiency of buildings: a review of knowledge, J. Energy Storage 27 (2020), 101083, https://doi.org/10.1016/j.est.2019.101083. Available from:.
[2] B. Kalidasan, A. Pandey, S. Shahabuddin, M. Samykano, R. Saidur, M. Thirugnanasam-bandam, Phase change materials integrated solar thermal energy systems: global trends and current practices in experimental approaches, J. Energy Storage 27 (2020), 101118, https://doi.org/10.1016/j.est.2019.101118. Available from:.
[3] Y. Dong, Y. Liu, D. Wang, Y. Wang, H. Du, J. Liu, Review of latent thermal energy storage systems for solar air-conditioning systems, Int. J. Energy Res. 44 (2) (2020) 669–707, https://doi.org/10.1002/er.4960. Available from:.
[4] E. Guelpa, V. Verda, Thermal energy storage in district heating and cooling systems: a review, Appl. Energy 252 (2019), 113474, https://doi.org/10.1016/j.apenergy.2019.113474. Available from:.
[5] Z. Li, Y. Lu, R. Huang, J. Chang, X. Yu, R. Jiang, et al., Applications and technological challenges for heat recovery, storage and utilization with latent thermal energy storage, Appl. Energy (2020), 116277, https://doi.org/10.1016/j.apenergy.2020.116277. Available from:.
[6] P. Moreno, C. Soĺ, A. Castell, L.F. Cabeza, The use of phase change materials in domestic heat pump and air-conditioning systems for short term storage: a review, Renew. Sustain. Energy Rev. 39 (2014) 1–13, https://doi.org/10.1016/j.rser.2014.07.062. Available from:.
[7] B. Al-Aifan, R. Parameshwaran, K. Mehta, R. Karunakaran, Performance evaluation of a combined variable refrigerant volume and cool thermal energy storage system for air conditioning applications, Int. J. Refrig. 76 (2017) 271–295, https://doi.org/10.1016/j.ijrefrig.2017.02.008. Available from:.
[8] J. Liu, Y. Liu, L. Yang, T. Liu, C. Zhang, H. Dong, Climatic and seasonal suitability of phase change materials coupled with night ventilation for office buildings in Western China, Renew. Energy 147 (2020) 356–373, https://doi.org/10.1016/j.renene.2019.08.069. Available from:.
[9] A. Wadhawan, A. Dhoble, V. Gawande, Analysis of the effects of use of thermal energy storage device (TESD) in solar air heater, Alex. Eng. J. 57 (3) (2018), 117383, https://doi.org/10.1016/j.aej.2017.03.016. Available from:.
[10] D. Mahon, P. Henshall, G. Claudio, P. Eames, Feasibility study of MgSO4+ zeolite based composite thermochemical energy stores charged by vacuum flat plate solar thermal collectors for seasonal thermal energy storage, Renew. Energy 145 (2020) 1799–1807, https://doi.org/10.1016/j.renene.2019.05.135. Available from:.
[11] L.F. Cabeza, L. Miró, E. Oró, A. de Gracia, V. Martin, A. Krönauer, et al., Mitigation accounting for thermal energy storage (TES) case studies, Appl. Energy 155 (2015) 365–377, https://doi.org/10.1016/j.apenergy.2015.05.121. Available from:.
[12] P. Arce, M. Medrano, A. Gil, E. Oró, L.F. Cabeza, Overview of thermal energy storage (TES) potential energy savings and climate change mitigation in Spain and Europe, Appl. Energy 88 (8) (2011) 2764–2774, https://doi.org/10.1016/j.apenergy.2011.01.067. Available from:.
[13] D.N. Nkwetta, F. Haghighat, Thermal energy storage with phase change material—a state-of-the-art review, Sustain. Cities Soc. 10 (2014) 87–100, https://doi.org/10.1016/j.scs.2013.05.007. Available from:.
[14] S. Wu, T. Yan, Z. Kuai, W. Pan, Thermal conductivity enhancement on phase change materials for thermal energy storage: a review, Energy Storage Mater. 25 (2020) 251–295, https://doi.org/10.1016/j.ensm.2019.10.010. Available from:.
[15] N. Tay, M. Belusko, F. Bruno, An effectiveness-NTU technique for characterizing tube-in-tank phase change thermal energy storage systems, Appl. Energy 91 (1) (2012) 309–319.
[16] R. Kothari, S.K. Sahu, S.I. Kundalwal, S. Sahoo, Experimental investigation of the effect of inclination angle on the performance of phase change material based finned heat sink, J. Energy Storage 37 (2021), 102462, https://doi.org/10.1016/j.est.2021.102462. Available from:.
[17] P. Larrinaga, G. Diarce, A. Campos-Celador, A. Garcia-Romero, Parametric characterization of a full-scale plate-based latent heat thermal energy storage system, Appl. Therm. Eng. 178 (2020), 115441, https://doi.org/10.1016/j.applthermaleng.2020.115441. Available from:.
[18] N. Stathopoulos, M. El Mankibi, R. Issoglio, P. Michel, F. Haghighat, Air–PCM heat exchanger for peak load management: experimental and simulation, Sol. Energy 132 (2016) 453–466, https://doi.org/10.1016/j.solener.2016.03.030. Available from:.
[19] T. Kumirai, J. Dirker, J. Meyer, Experimental analysis for thermal storage performance of three types of plate encapsulated phase change materials in air heat exchangers for ventilation applications, J. Build. Eng. 22 (2019) 75–89, https://doi.org/10.1016/j.jobe.2018.11.016. Available from:.
[20] X. Xiao, P. Zhang, M. Li, Preparation and thermal characterization of paraffin/metal foam composite phase change material, Appl. Energy 112 (2013) 1357–1366, https://doi.org/10.1016/j.apenergy.2013.04.050. Available from:.
[21] R.M. Saeed, J.P. Schlegel, R. Sawafta, V. Kalra, Plate type heat exchanger for thermal energy storage and load shifting using phase change material, Energy Convers. Manag. 181 (2019) 120–132, https://doi.org/10.1016/j.enconman.2018.12.013. Available from:.
[22] W. Lin, W. Zhang, Z. Ling, X. Fang, Z. Zhang, Experimental study of the thermal performance of a novel plate type heat exchanger with phase change material, Appl. Therm. Eng. 178 (2020), 115630, https://doi.org/10.1016/j.applthermaleng.2020.115630. Available from:.
[23] B. Gürel, A numerical investigation of the melting heat transfer characteristics of phase change materials in different plate heat exchanger (latent heat thermal energy storage) systems, Int. J. Heat Mass Transf. 148 (2020), 119117, https://doi.org/10.1016/j.ijheatmasstransfer.2019.119117. Available from:.
[24] A.K. Raj, M. Srinivas, S. Jayaraj, Transient CFD analysis of macro encapsulated latent heat thermal energy storage containers incorporated within solar air heater, Int. J. Heat Mass Transf. 156 (2020), 119896, https://doi.org/10.1016/j.ijheatmasstransfer.2020.119896. Available from:.
[25] B. Gürel, V.R. Akkaya, M. Göltaş, Ç.N. Şen, O.V. Gürel, M.I. Koşar, et al., Investigation on flow and heat transfer of compact brazed plate heat exchanger with lung pattern, Appl. Therm. Eng. 175 (2020), 115309, https://doi.org/10.1016/j.applthermaleng.2020.115309. Available from:.
[26] A. Sözen, A. Khanlari, Experimental and numerical investigation of nanofluid usage in a plate heat exchanger for performance improvement, Available from, Int. J. Renew. Energy Dev. 8 (1) (2019) 27–32, https://doi.org/10.14710/ijred.8.1.27-32.
[27] G. Nouri, Y. Noorollahi, H. Yousefi, Designing and optimization of solar assisted ground source heat pump system to supply heating, cooling and hot water demands, Geothermics 82 (2019) 212–231, https://doi.org/10.1016/j.geothermics.2019.06.011. Available from:.
[28] S. Minetto, Theoretical and experimental analysis of a CO2 heat pump for domestic hot water, Int. J. Refrig. 34 (3) (2011) 742–751, https://doi.org/10.1016/j.ijrefrig.2010.12.018. Available from:.

[29] P.R. Bobbili, B. Sunden, S.K. Das, An experimental investigation of the port flow maldistribution in small and large plate package heat exchange- ers, Appl. Therm. Eng. 26 (16) (2006) 1919–1926, https://doi.org/10.1016/j.applthermaleng.2006.01.015. Available from:.
[30] N.K. Panday, S.N. Singh, Experimental study of flow and thermal behavior in single and multi-pass chevron-type plate heat exchangers, Chem. Eng. Process. Process Intensif. 171 (2022), 108758, https://doi.org/10.1016/j.cep.2021.108758. Available from:.
[31] M.K. Bassiouny, H. Martin, Flow distribution and pressure drop in plate heat exchangers—I U-type arrangement, Chem. Eng. Sci. 39 (4) (1984) 693–700, https://doi.org/10.1016/0009-2509(84)80176-1. Available from:.
[32] M. Bassiouny, H. Martin, Flow distribution and pressure drop in plate heat exchangers—II Z-type arrangement, Chem. Eng. Sci. 39 (4) (1984) 701–704, https://doi.org/10.1016/0009-2509(84)80177-3. Available from:.
[33] M. Abdoly, D. Rapp, Theoretical and experimental studies of stratified thermocline storage of hot water, Energy Convers. Manag. 22 (3) (1982) 275–285, https://doi.org/10.1016/0196-8904(82)90053-X. Available from:.
[34] M. Liu, N. Tay, M. Belusko, F. Bruno, Investigation of cascaded shell and tube latent heat storage systems for solar tower power plants, Energy Procedia 69 (2015) 913–924.
[35] R.B. Bird, W.E. Stewart, E.N. Lightfoot, Diffusivity and the mechanisms of mass transport, in: Transport Phenomena, 1960, pp. 495–518.
[36] J Wang H Xie Z Xin. Thermal properties of paraffin-based composites containing multi-walled carbon nanotubes. Thermochem.Acta. 009;488(1-2):39-42. Available from: doi:10.1016/j.tca.2009.01.022.
[37] A.K. Raj, M. Srinivas, S. Jayaraj, Transient CFD analysis of macro-encapsulated latent heat thermal energy storage containers incorporated within solar air heater, Int. J. Heat Mass Transf. 156 (2020), 119896, https://doi.org/10.1016/j.ijheatmasstransfer.2020.119896. Available from:.
[38] M. Akgün, O. Aydın, K. Kaygusuz, Experimental study on melting/solidification characteristics of a paraffin as PCM, Energy Convers. Manag. 48 (2) (2007) 669–678, https://doi.org/10.1016/j.enconman.2006.05.014. Available from:.
[39] C. Prakash, M. Samonds, A. Singhal, A fixed grid numerical methodology for phase change problems involving a moving heat source, Int. J. Heat Mass Transf. 30 (12) (1987) 2690–2694, https://doi.org/10.1016/0017-9310(87)90152-9. Available from: https.
[40] F. Tan, S. Hosseinizadeh, J. Khodadadi, L. Fan, Experimental and computational study of constrained melting of phase change materials (PCM) inside a spherical capsule, Int. J. Heat Mass Transf. 52 (15–16) (2009) 3464–3472, https://doi.org/10.1016/j.ijheatmasstransfer.2009.02.043. Available from:.
[41] Bouhal T, Fertahi S, Agrouaz Y, El Rhafiki T, Kousksou T, Jamil A. Numerical modeling and optimization of thermal stratification in solar hot.
[42] P.S. Ghoshdastidar, 5.13 Heat Transfer in Laminar Tube Flow, Available from:, Oxford University Press, 2012 https://app.knovel.com/hotlink/khtml/id:kt00TVI7K9/heat-transfer-2nd-edition/heat-transfer-in-laminar.